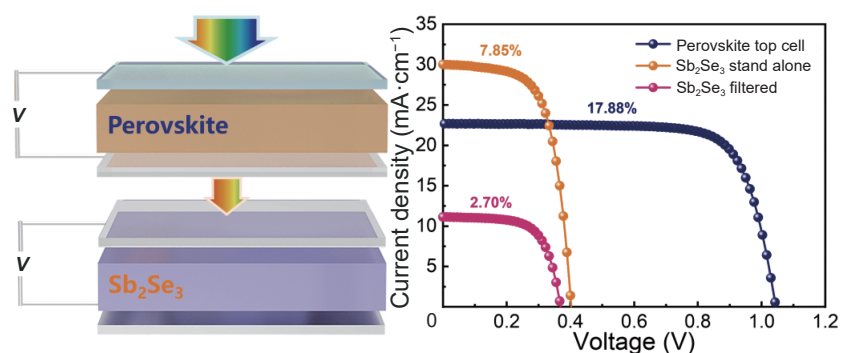**Research Article**

# Sb$_2$Se$_3$ as a bottom cell material for efficient perovskite/Sb$_2$Se$_3$ tandem solar cells

Zhiyuan Cai, Jia Sun, Huiling Cai, Yuehao Gu, Rongfeng Tang, Changfei Zhu, Paifeng Luo ✉, and Tao Chen ✉

## Graphical Abstract

✉Address correspondence to
Paifeng Luo, lpfeng@hfut.edu.cn;
Tao Chen, tchenmse@ustc.edu.cn

🔗 Read Online

↗ Submit Online

In this study, we demonstrate a proof-of-concept tandem solar cell composed of antimony selenide and wide-band-gap perovskite as bottom and top subcell absorption materials. This device achieves >20% power conversion efficiency by optimizing the transparent electrode of the top cell and the preparation process of the bottom cell.

# Sb$_2$Se$_3$ as a bottom cell material for efficient perovskite/Sb$_2$Se$_3$ tandem solar cells

Zhiyuan Cai[1,†], Jia Sun[2,†], Huiling Cai[1], Yuehao Gu[1], Rongfeng Tang[1], Changfei Zhu[1], Paifeng Luo[2] ✉, and Tao Chen[1] ✉

[1] Hefei National Research Center for Physical Sciences at the Microscale, CAS Key Laboratory of Materials for Energy Conversion, School of Chemistry and Materials Science, University of Science and Technology of China, Hefei 230026, China

[2] School of Materials Science and Engineering, Hefei University of Technology, Hefei 230026, China

[†] Zhiyuan Cai and Jia Sun contributed equally to this work.

## ABSTRACT

Antimony selenide (Sb$_2$Se$_3$) semiconducting material possesses a band gap of 1.05–1.2 eV and has been widely applied in single-junction solar cells. Based on its band gap, Sb$_2$Se$_3$ can also be used as the bottom cell absorber material in tandem solar cells. More importantly, Sb$_2$Se$_3$ solar cells exhibit excellent stability with nontoxic compositional elements. The band gap of organic–inorganic hybrid perovskite is tunable over a wide range. In this work, we demonstrate for the first time a perovskite/antimony selenide four-terminal tandem solar cell with a specially designed and fabricated transparent electrode for an optimized spectral response. By adjusting the thickness of the transparent electrode layer of the top cell, the wide-band-gap perovskite top solar cell achieves an efficiency of 17.88%, while the optimized antimony selenide bottom cell delivers a power conversion efficiency of 7.85% by introducing a double electron transport layer. Finally, the four-terminal tandem solar cell achieves an impressive efficiency exceeding 20%. This work provides a new tandem device structure and demonstrates that antimony selenide is a promising absorber material for bottom cell applications in tandem solar cells.

## 1 Introduction

With the development of material fabrication, device structure design, and construction, photovoltaic technology has gained remarkable achievement. In some conventional solar cells, such as Si, Cu(In,Ga)Se$_2$, CdTe, and organic–inorganic perovskite, laboratory studies have achieved power conversion efficiencies (PCE) of over 20% in single-junction solar cells[1]. The PCE of the intensely developed devices has been quite close to the Shockley–Queisser limit (S–Q limit)[2, 3]. In this regard, further increase in efficiency requires exponentially increased efforts and costs. An alternative way to overcome the S–Q limit in single-junction

solar cells is the fabrication of tandem solar cells. Tandem solar cells broaden the spectral response of the cell and maximize the use of solar energy, thereby improving the theoretical efficiency to 46% in a double-heterojunction solar cell. Double-junction tandem solar cells can adopt a two-terminal (2-T) configuration by serially connecting two subcells through an interlayer, which requires delicate band gap matching between the top and bottom cells and specially designed interfacial materials. However, in the mechanically stacked four-terminal (4-T) configuration, band gap matching and interfacial engineering exhibit high flexibility. In principle, for the bottom and top cells with band gaps of ~1.2 and

~1.6 eV, the 4-T configuration can achieve a theoretical PCE above 40%[4].

As a promising light-harvesting material in photovoltaic devices, antimony selenide ($Sb_2Se_3$) has attracted increasing interest in solar cell applications[5]. It is a binary semiconducting material with a single stable orthorhombic phase, composed of low-cost and nontoxic Sb and Se elements. Antimony selenide also possesses a high absorption coefficient ($>10^5$ $cm^{-1}$ at visible wavelength) and a narrow bandgap (1.05–1.2 eV)[6]. Owing to the high absorption coefficient, the film thickness of $Sb_2Se_3$ in the order of several hundred nanometers can guarantee sufficient light harvesting. Past research focused mainly on fundamental property investigations and applications in single-junction solar cells. From the band gap perspective, $Sb_2Se_3$ is a suitable bottom cell material for tandem solar cells.

In this study, we demonstrate a proof-of-concept tandem device structure using $Sb_2Se_3$ as the bottom cell material and a wide-bandgap organic–inorganic hybrid perovskite material as the top cell material. We focus on the critical challenges of this new device structure. In the top cell, the transparent conducting electrode (TCE) plays a critical role as both a charge collection electrode and transmits light of the near-infrared (NIR) part into the bottom cells. The TCE of top cells must exhibit low resistance, high light transmittance, protection against oxygen and moisture, and good chemical stability[7, 8]. Indium-doped tin oxide (ITO)[9], indium-doped zinc oxide (IZO)[10], aluminum-doped zinc oxide (AZO)[11], and hydrogenated indium oxide (ICO:H)[12] are common transparent conducting electrodes in semitransparent PSCs. Here, we apply IZO films as transparent conducting electrodes in semitransparent PSCs because of their lower parasitic NIR absorption, high mobility, high light transmittance, and low fabrication temperature. We developed a method to balance the conductivity and transmittance of transparent conductive films, obtaining a high efficiency of >17%. By introducing a double electron-transporting layer in the bottom cell material, the crystallographic orientation of the antimony selenide film is optimized, which enhances the carrier transport and finally achieves a PCE of 7.85%. Subsequently, we assembled a 4-T tandem solar cell by mechanically stacking the two subcells. The top perovskite solar cell with a wide bandgap can absorb light in the wavelength range of 300–800 nm, while allowing lower-energy photons to pass through and get absorbed by the bottom antimony selenide solar cell. Ultimately, we fabricated a novel perovskite/$Sb_2Se_3$ 4-T tandem solar cell with the PCE exceeding 20%, indicating the effectiveness of this new tandem device structure.

## 2    Fabrication of IZO electrode for the perovskite top cell

The band gap of perovskite material can be continuously adjusted within 1.48–2.23 eV, making it an ideal candidate for the top or bottom layer of series solar cells[13–15]. Here, we applied a wide-band-gap perovskite as the top cell material. In typical perovskite film synthesis, we dissolved formamidinium (FA), methylammonium (MA), and $PbI_2$ in a mixture of dimethyl formamide (DMF) and dimethylsulfoxide (DMSO), which was spin-coated onto FTO/$TiO_2$ substrates with further annealing at 120°C for 20 min. The synthetic details are described in the experimental section. The as-prepared perovskite showed a stoichiometry of $FA_{0.85}MA_{0.15}PbI_3$, and the bandgap of the as-prepared perovskite was calculated as approximately 1.58 eV (Fig. S1).

Before device fabrication, we studied the relationship between thickness and transparency and the conductivity of the IZO electrode for efficient device fabrication. Here, we applied the magnetron sputtering method to prepare transparent IZO with different thicknesses on quartz glass. As shown in Figs. 1a and 1b, the resistivity and sheet resistance of the IZO layer decreased with the increasing thickness of IZO from 200 to 500 nm. However, when the thickness was increased to 500 nm, the film mobility decreased slightly (Fig. 1c). A suitable TCE should have high conductivity and transmittance. Thus, we examined the light transmittance of TCEs with different thicknesses (Fig. 1d). The average transmittance of the IZO layer with thicknesses of 200, 300, and 400 nm exceeded 85% in the 400–1200 nm wavelength range, showing a slight decrease with the increasing IZO thickness. The corresponding parameters are summarized in Table 1 for easy comparison.

The NIR transmittance of the complete semitransparent top cells directly affects the light absorption of the bottom cells, thus influencing the photovoltaic performance of the bottom cells. We then examined the light transmittance of the semitransparent top cell based on the fabricated perovskite films (Fig. 2a). We introduced a $MoO_3$ buffer layer on the perovskite layer through thermal evaporation to protect it from damage during the subsequent IZO sputtering process[16, 17]. Except for those with the IZO thickness of 500 nm, the samples with the IZO thicknesses of 200, 300, and 400 nm maintained high transmittance in the wavelength range of 800–1200 nm, wherein the average value is above 80%. Furthermore, we studied the effect of different IZO thicknesses on the photovoltaic performance of semitransparent perovskite solar cells (ST-PSC); the device structure is described as FTO/$TiO_2$/perovskite/$MoO_3$/IZO. The current density–voltage curves and the corresponding photo-
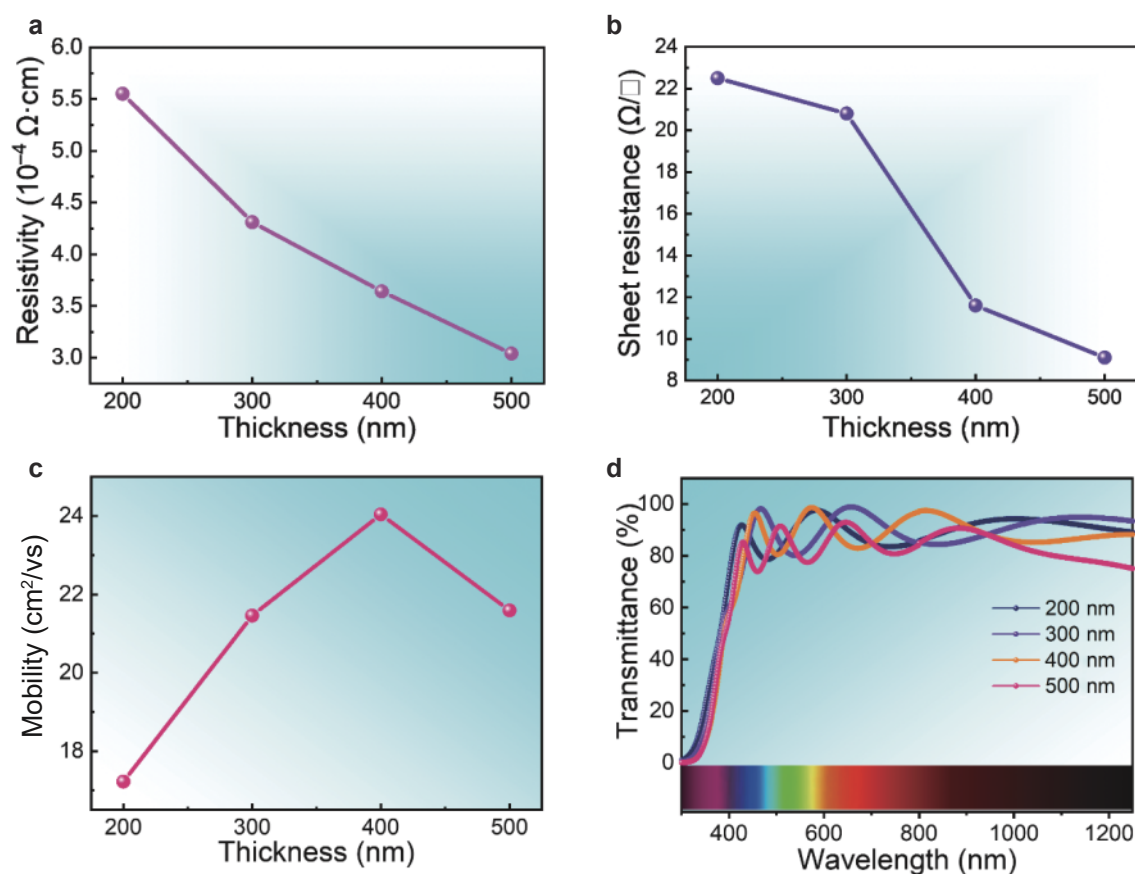
**Figure 1** Electrical and optical characterizations of the as-deposited IZO films. (a) Resistivity, (b) sheet resistance, (c) carrier mobility, and (d) transmittance of the IZO films with thicknesses of 200, 300, 400, and 500 nm.

**Table 1** Typical values of sheet resistance, mobility, resistivity, and average transmittance of IZO samples of different thicknesses

| Thickness of the IZO (nm) | 200 | 300 | 400 | 500 |
|---|---|---|---|---|
| Resistivity ($10^{-4}$ $\Omega$·cm) | 5.55 | 4.31 | 3.64 | 3.04 |
| Sheet resistance ($\Omega/\square$) | 22.5 | 20.8 | 11.6 | 9.1 |
| Mobility (cm²/vs) | 17.22 | 21.46 | 24.04 | 21.59 |
| Average transmittance in 400–1200 nm (%) | 89.7 | 89.4 | 88.3 | 83.6 |

voltaic parameters are shown in Fig. 2b and Table 2, respectively. When the thickness of the IZO film was 200 nm, the device delivered a PCE of 15.25%, with the fill factor (FF) and short-circuit current density ($J_{SC}$) and open-circuit voltage ($V_{OC}$) of 69.26%, 22.36 mA/cm², and 0.98 V, respectively. When the thickness of the IZO film was increased to 400 nm, the PCE reached 17.88%, with notable increases in FF and $J_{SC}$ to 75.54% and 22.68 mA/cm², respectively. The decreased resistivity and sheet resistance of the TCE contributed to this performance improvement. However, once the transparent electrode thickness was further increased to 500 nm, the device performance decreased slightly, with PCE and FF dropping to 17.00% and 70.29%, respectively. This performance degradation was possibly due to the reduced carrier mobility when the IZO film thickness reached 500 nm. The current density–voltage curves of the reverse and forward voltage scans of the champion

semitransparent perovskite solar cells are shown in Fig. 2c, which showed minimal hysteresis, with reverse- and forward-scan PCEs of 17.88% and 16.37%, respectively. In addition, steady-state output at the maximum power point (MPP) was performed (Fig. 2d). After 100 s of measurement, the stable-state output efficiencies of the semitransparent PSCs were 17.0%. The steady-state PCEs of the devices could maintain over 95% maximum efficiency, indicating the reliability of the device structure and the device fabrication method.

## 3 Enhancing the device performance of antimony selenide subcells using a double electron transport layer

Antimony selenide has a unique quasi-one-dimensional structure (Figs. 3a and 3b), wherein efficient carrier transport occurs along the one-dimensional
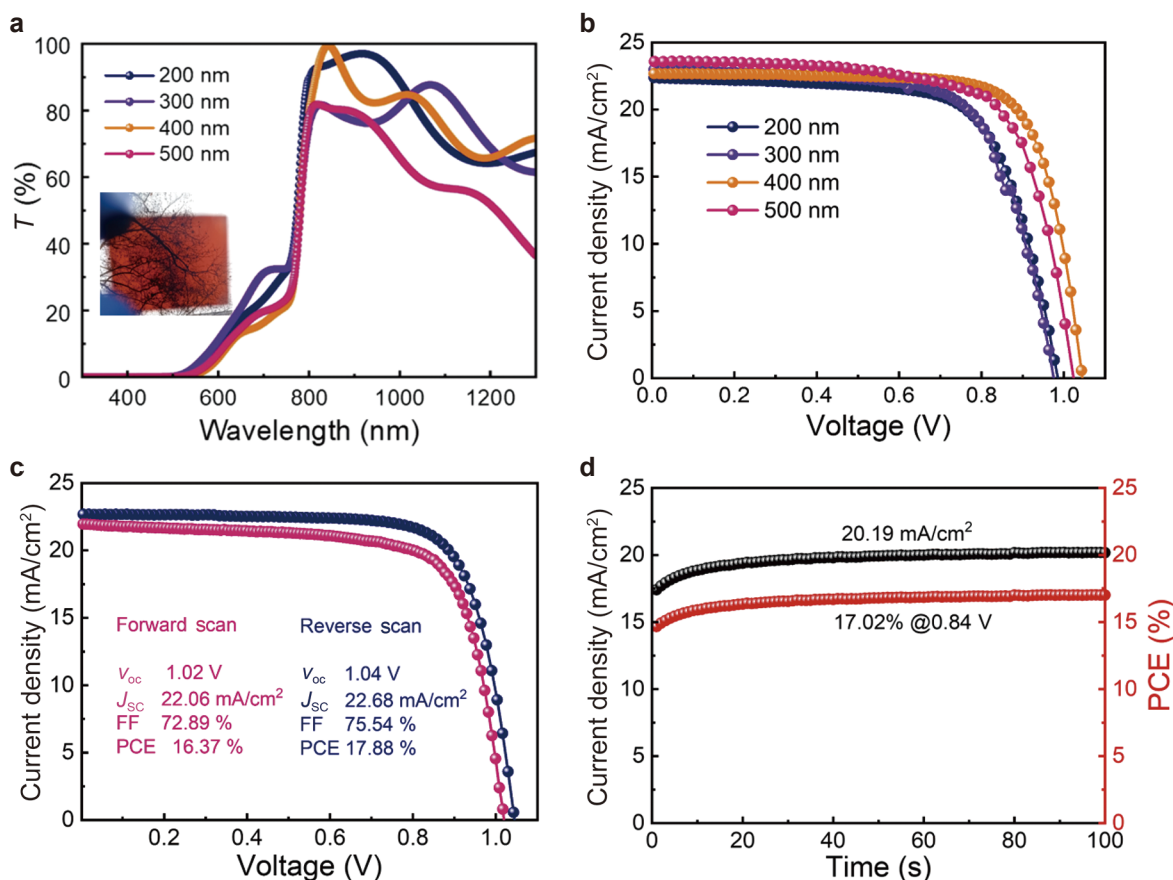
**Figure 2**  Performance of the semitransparent top cell. (a) Transmittance of semitransparent top cells with different IZO thicknesses from 200 to 500 nm. (b) Current density–voltage curves of devices with different IZO thicknesses. (c) Current density–voltage curves of reverse and forward voltage scans of the best semitransparent perovskite solar cells. (d) MPP tracking of PSCs under continuous AM 1.5 G illumination.

**Table 2**  Performance parameters of the semi-transparent perovskite top cell corresponding to different IZO thicknesses from 200 to 500 nm

| Thickness of the IZO (nm) | $V_{OC}$ (V) | $J_{SC}$ (mA/cm²) | FF (%) | PCE (%) |
|---|---|---|---|---|
| 200 | 0.98 | 22.36 | 69.26 | 15.25 |
| 300 | 0.97 | 22.97 | 68.61 | 15.35 |
| 400 | 1.04 | 22.68 | 75.54 | 17.88 |
| 500 | 1.02 | 23.62 | 70.29 | 17.00 |

chain of [hk1] crystal direction[18–22]. Therefore, the crystal orientation of the $Sb_2Se_3$ thin film has a prominent influence on device performance[23]. Here, we introduced the $SnO_2$/CdS double electron transport layers (ETLs) in the device, which was synthesized using the spin coating method. This double ETL could improve the flatness of the electron-transporting layer and optimize the orientation of the absorber layer.

To investigate the quality of the as-prepared $SnO_2$ layer, we conducted scanning electron microscopy (SEM) characterization of the surface of the FTO/$SnO_2$ film (Fig. 3c). Compared with the clean FTO surface morphology (shown in Fig. S2), after the annealing of the as-fabricated $SnO_2$ nanoparticle layer, a compact $SnO_2$ film was formed on the FTO

surface. Unlike the bare FTO surface, the $SnO_2$ layer provided a smoother substrate for the subsequent deposition of CdS via chemical bath deposition (CBD). According to the cross-sectional SEM images of the sample after the deposition of CdS via CBD (Fig. 3d), the $SnO_2$/CdS double ETLs were intimately bound without distinguishable interfaces, and the total thickness was estimated as 70 nm. Furthermore, with the introduction of the $SnO_2$ layer, the root-mean-square roughness ($R_q$) of the electron-transporting layer surface decreased from 38.2 to 31.2 nm (Figs. 3e and 3f).

Subsequently, the $Sb_2Se_3$ absorption layer was prepared on top of either single or double ETLs via thermal evaporation at a substrate temperature of 355°C by using $Sb_2Se_3$ powder as the precursor mate-
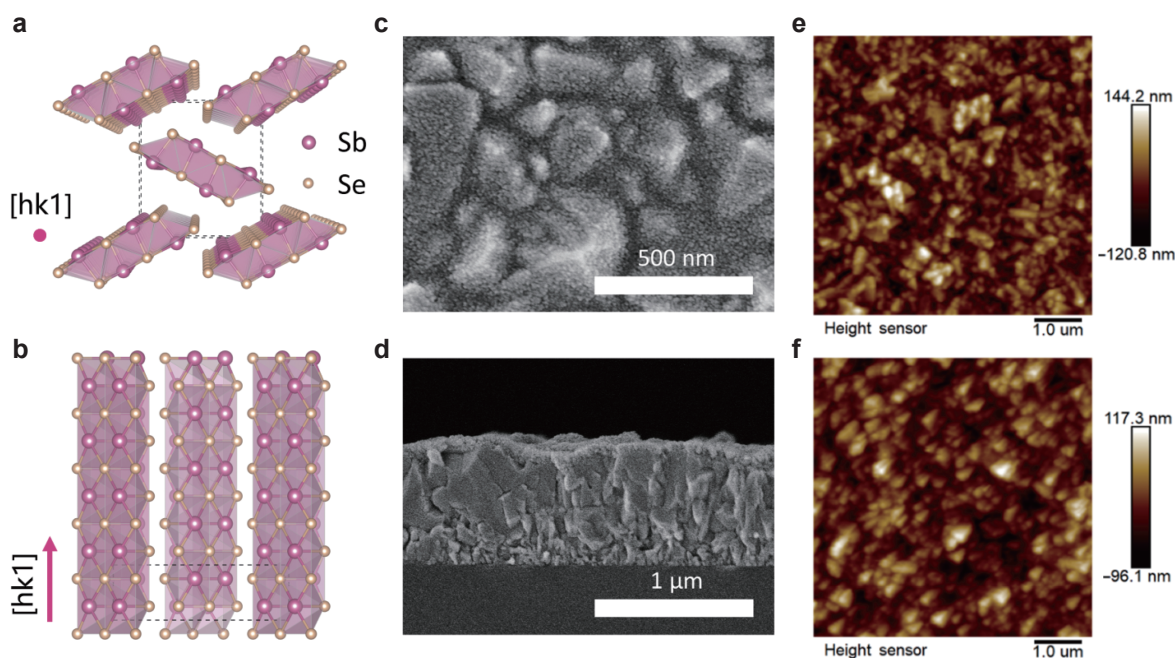
**Figure 3** Diagram of the Sb$_2$Se$_3$ crystal structure (a) perpendicular and (b) parallel to the [hk1] orientation. (c) Surface SEM image of FTO/SnO$_2$ thin film and (d) cross-sectional SEM image of the FTO/SnO$_2$/CdS thin film. Atomic force microscopy images of the (e) FTO/CdS film and (f) FTO/SnO$_2$/CdS film. The scan area is 6 μm × 6 μm.

rial. The crystal structure (Fig. 4a) was similar to that of orthorhombic Sb$_2$Se$_3$ (PDF#89-0821). To examine the preferential crystal orientation, we calculated the texture coefficient (TC$_{(hkl)}$) of the two types of Sb$_2$Se$_3$ films. The results (Fig. 4b) illustrated that Sb$_2$Se$_3$ film grown on the SnO$_2$/CdS double electron-transporting layer has a higher relative intensity of the peaks (hkl) (l ≠ 0) than those on the CdS ETL in the absence of the SnO$_2$ interlayer.

To illustrate how the film characteristics influence device efficiency, we fabricated a superstrate device configuration described as Glass/FTO/CdS/Sb$_2$Se$_3$/Spiro-OMeTAD/Au. The current density–voltage curves of the two devices are shown in Fig. 4c. The Sb$_2$Se$_3$ device with a single ETL delivered a PCE of 7.10%, with an FF, a $J_{SC}$, and a $V_{OC}$ of 57.96%, 29.73 mA/cm$^2$, and 0.412 V, respectively. Meanwhile, the device with double ETLs delivered a PCE of 7.85%, with an FF, a $J_{SC}$, and a $V_{OC}$ of 59.85%, 30.86 mA/cm$^2$, and 0.426 V, respectively. The introduction of double ETLs led to a more optimal [hk1] crystal orientation of the Sb$_2$Se$_3$ layer, thereby improving the carrier transport capability. Furthermore, the smoother ETL surface improved the ETL/Sb$_2$Se$_3$ heterojunction quality, thus reducing the leakage current of the device. This optimization improved the FF, $V_{OC}$, and $J_{SC}$ of the device and, finally, the PCE from 7.1% to 7.85%. The statistical PCE of 10 devices each for the SnO$_2$/CdS double ETL and the CdS ETL Sb$_2$Se$_3$ devices are illustrated in Fig. 4d. The devices with a double ETL showed remarkably improved performance with good repeatability, indicating that this processing is highly reliable.

## 4 Four-terminal perovskite/Sb$_2$Se$_3$ tandem solar cells

A schematic of the 4-T perovskite/Sb$_2$Se$_3$ tandem solar cell is displayed in Fig. 5a, wherein short-wavelength photons are well captured by the perovskite top subcell, whereas long-wavelength photons pass through the top cell into the Sb$_2$Se$_3$ bottom subcell. The cross-sectional SEM images of a Sb$_2$Se$_3$ bottom subcell with a FTO/SnO$_2$/CdS/Sb$_2$Se$_3$/Spiro-OMeTAD/Au structure and a top semitransparent PSC subcell with an n-i-p structure consisting of FTO/SnO$_2$/Perovskite/Spiro-OMeTAD/MoO$_3$/IZO are shown in Figs. 5b and 5c, respectively. Figure 5d depicts the current density–voltage curves of the perovskite top cell with an IZO layer thickness of 400 nm, the Sb$_2$Se$_3$ cell, and the filtered Sb$_2$Se$_3$ cell. The corresponding photovoltaic parameters are summarized in Table S1. The semitransparent perovskite top cell generated a PCE of 17.88%, a $V_{OC}$ of 1.04 V, a $J_{SC}$ of 22.68 mA cm$^{-2}$, and an FF of 75.54%. The standalone Sb$_2$Se$_3$ cell delivered a PCE of 7.85%, a $V_{OC}$ of 0.40 V, a $J_{SC}$ of 30.01 mA cm$^{-2}$, and an FF of 64.96%. Because the top cell absorbed most short wavelengths, the PCE of the Sb$_2$Se$_3$ bottom cell decreased to 2.70% after being filtered by the perovskite top cell, with a $V_{OC}$ of 0.37 V, a $J_{SC}$ of 11.12 mA cm$^{-2}$, and an FF of 65.77%. Consequently, the 4-T perovskite/Sb$_2$Se$_3$ tandem cell achieved a summed PCE of 20.58%.

We also tested the photovoltaic performance of 4-T tandem cells with different IZO film thicknesses. With the increase in the IZO thickness of the top cell,
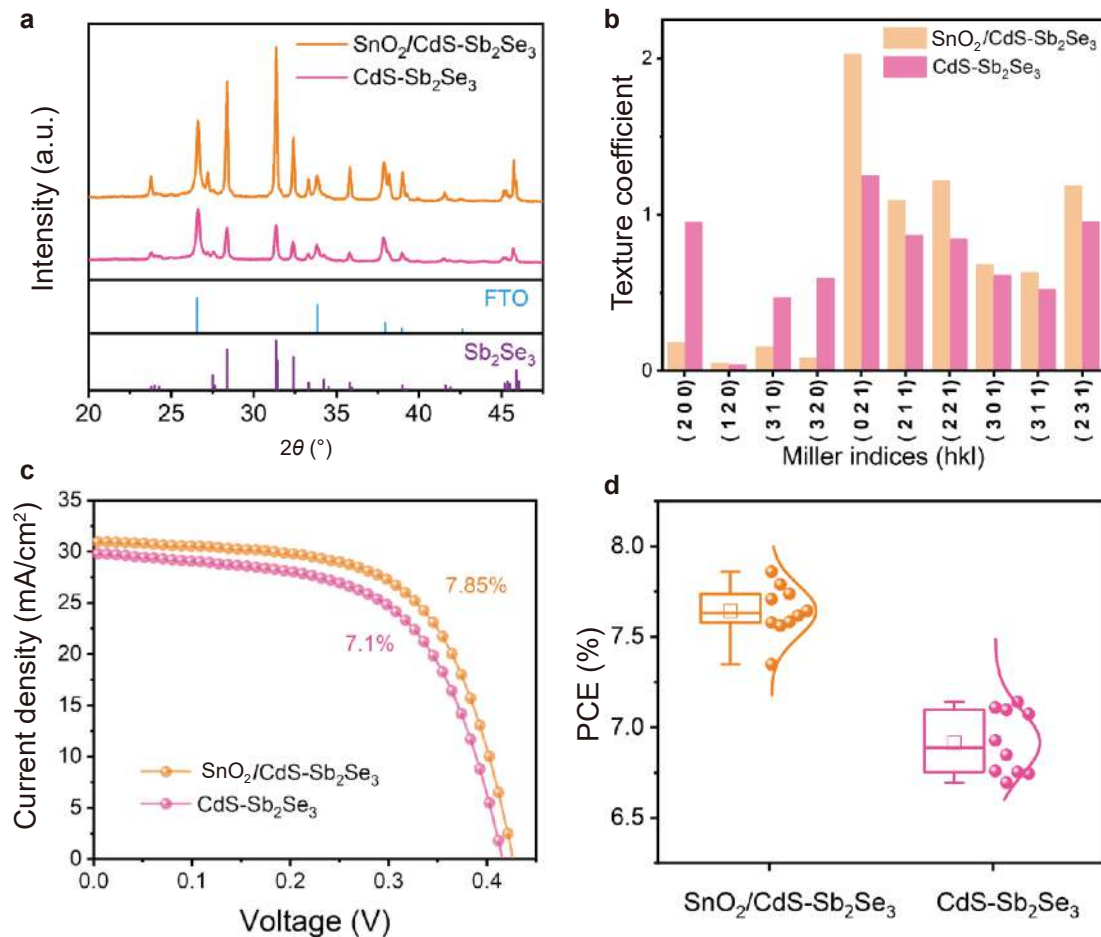
**Figure 4**   Structure and device performance of the $Sb_2Se_3$ films. (a) X-ray diffraction patterns and (b) the corresponding calculated texture coefficient, (c) current density–voltage curves, and (d) statistical boxplots of PCE for $SnO_2/CdS$-$Sb_2Se_3$ and $CdS$-$Sb_2Se_3$ solar cells.

the light absorption of the $Sb_2Se_3$ bottom cell, in turn, gradually decreased, resulting in a drop in the $J_{SC}$ from 12.23 to 10.90 mA cm$^{-2}$ and eventually the PCE of the filtered bottom cell decreased from 2.94% to 2.57%. When the IZO film thicknesses of the perovskite top cells were 200, 300, and 400 nm, the overall efficiencies of tandem solar cells were 18.19%, 18.10%, and 19.57%, respectively.

The spectrum responses of the semitransparent perovskite top cell, $Sb_2Se_3$ cell, and filtered $Sb_2Se_3$ bottom cell subcells were examined through external quantum efficiency (EQE) (Fig. 5e). The top and bottom cells showed the onset absorption wavelengths of approximately 800 and 1050 nm, respectively. Therefore, the 4-T perovskite/$Sb_2Se_3$ tandem cells greatly improved the utilization of the solar spectrum. Furthermore, the CdS ETL is widely used in $Sb_2Se_3$ solar cells because of its better interfacial compatibility with the $Sb_2Se_3$ film, while the band gap of CdS is narrow at approximately 2.42 eV, leading to the parasitic absorption in the visible-light region from 350 to 500 nm. When $Sb_2Se_3$ is used in the bottom cell of the tandem solar cell, because the top cell will preabsorb and utilize the photon energy of

the short-wavelength region, it avoids the negative impact of CdS parasitic absorption on device performance. This observation also provides a new strategy for reducing the parasitic absorption of CdS in $Sb_2Se_3$ solar cells.

## 5   Conclusion

In summary, we successfully fabricated 4-T perovskite/$Sb_2Se_3$ tandem solar cells. The IZO films prepared through magnetron sputtering generate both good conductivity and outstanding transparency. By optimizing the thickness of the IZO transparent contact, we prepared a semitransparent top cell with a PCE of 17.88% and an average transmission of approximately 70% for photons with wavelengths ranging from 800 to 1100 nm. Meanwhile, the crystal orientation of the antimony selenide film was optimized by introducing a $SnO_2/CdS$ double electron-transporting layer, and the PCE of the $Sb_2Se_3$ device improved from 7.1% to 7.85%. Ultimately, the PCE of the 4-T perovskite/$Sb_2Se_3$ tandem solar cells reached 20.58%, which is higher than that of the independent subcells.
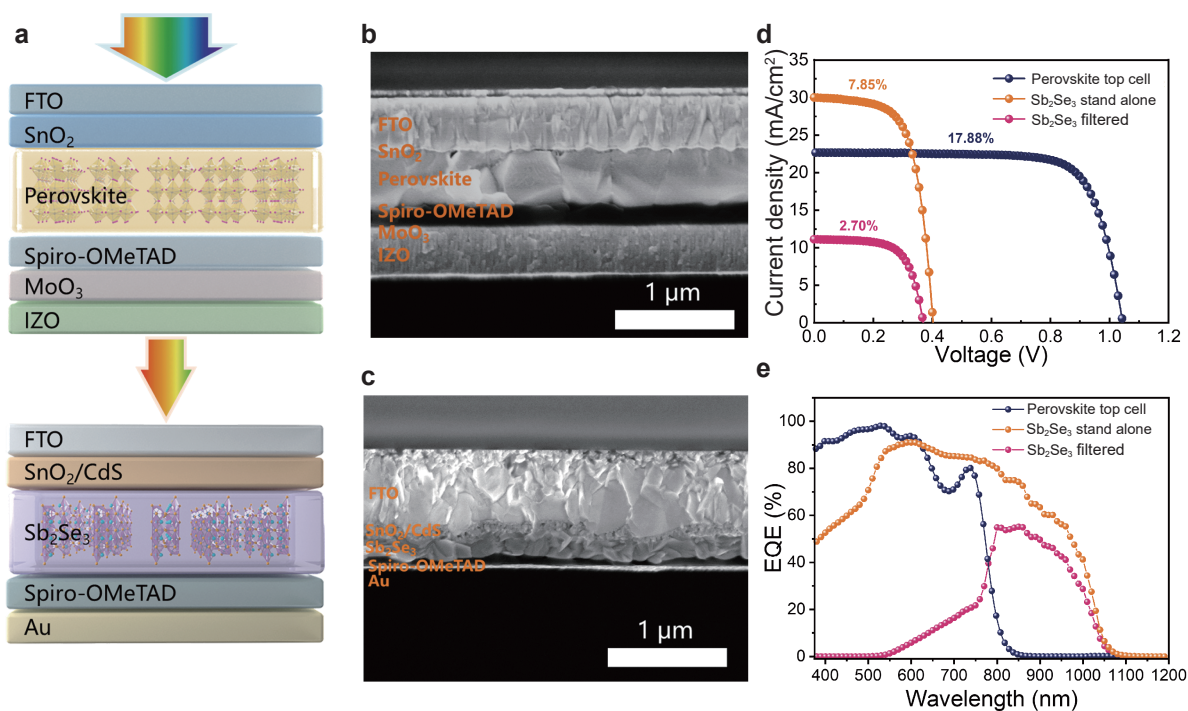
**Figure 5** Characterization of perovskite/antimony selenide four-terminal tandem solar cells. (a) Schematic illustration of the perovskite/antimony selenide tandem solar cell, cross-sectional SEM images of (b) semitransparent perovskite top cell and (c) antimony selenide bottom cell. (d) Current density–voltage curves of the semitransparent perovskite top cell with an IZO thickness of 400 nm, unfiltered antimony selenide solar cell, and antimony selenide solar cell filtered by the semitransparent top cell. (e) EQE of the best semitransparent perovskite top cell with an IZO thickness of 400 nm, unfiltered antimony selenide bottom cell, and antimony selenide bottom cell filtered by the top cell.

This study shows that antimony selenide has great potential for bottom cell applications.

# 6   Experimental section

**Semi-transparent perovskite top cell fabrication:** $SnO_2$ colloid precursors were diluted with deionized water at a volume ratio of 1:6.5 and then spin-coated on FTO glasses at 3000 r/min for 30 s and annealed at 500°C for 30 min in air. The perovskite precursors (1.35 mol L$^{-1}$) were prepared by dissolving MAI, FAI, and $PbI_2$ in 1 mL DMF/DMSO ($v/v$ = 4:1) and later stirred at 70°C for 2 h. Then, the perovskite precursors were spin-coated on $SnO_2$/FTO substrates at 1000 r/min for 10 s and 4000 r/min for 30 s. During the second step, 110 µL ethyl acetate was dropped onto the films in the last 15 s. Subsequently, the perovskite films were annealed at 120°C for 20 min in ambient air (30%–40% humidity). The Spiro-OMeTAD precursor solutions were prepared by dissolving 70 mg of Spiro-OMeTAD in 1 mL of chlorobenzene with the additives of 28 µL TBP and 17.5 µL Li-TFSI. The Spiro-OMeTAD precursor solutions were spin-coated at 4000 r/min for 30 s. $MoO_3$ was deposited on the samples via thermal evaporation under a high vacuum of $3 \times 10^{-4}$ Pa. The rear transparent contact was then fabricated by sputtering IZO on $MoO_3$. The IZO layer was deposited via radio-frequency magnetron sputtering on top of

$MoO_3$ at a deposition pressure of 0.3 Pa with an Ar flow of 60 sccm.

**Antimony selenide bottom cell fabrication:** $SnO_2$/CdS double electron-transporting layer was prepared using a two-step method. In particular, the FTO-coated glass was cleaned with deionized water, isopropanol, acetone, and ethanol for 40 min via ultrasonication. The $SnO_2$ dispersion solution was mixed with deionized water in a volume ratio of 1:5 and stirred for 24 h. It was then spin-coated onto the FTO surface at 3000 r/min for 30 s, followed by annealing in air at 250°C for 30 min. Subsequently, the CdS film was deposited in a solution containing $CdSO_4$ (0.015 mol L$^{-1}$), thiourea (1.50 mol L$^{-1}$), and ammonia (28%) at 66°C for 16 min. Then, $SbCl_3$ methanol solution (30 mg mL$^{-1}$) was coated onto the CdS surface at 3000 r/min for 30 s, followed by annealing in air at 400°C for 10 min.

The preparation method of the single CdS electron-transporting layer is similar to that of the double electron-transporting layer, grown directly on the cleaned FTO through chemical bath deposition and annealed after spin coating with $SbCl_3$ methanol solution.

The antimony selenide layer was fabricated using vacuum thermal evaporation under a vacuum pressure of $5.0 \times 10^{-4}$ Pa. The high-purity $Sb_2Se_3$ (99.999%, Jiangxi Ketai) evaporated at an evapora-

tion rate of 80–120 nm s⁻¹ and deposited on glass/FTO/SnO₂/CdS and glass/FTO/CdS substrates. The substrate temperature was controlled at 345°C, and the film thickness was controlled at approximately 300 nm. The deposited antimony selenide films were then transferred into a nitrogen-filled glove box for postannealing. The optimized post-annealing condition was 370°C for 8 min.

The Spiro-OMeTAD layer and Au contact were deposited according to a reported method[24]. The Spiro-OMeTAD solution was prepared by mixing 36.6 mg of Spiro-OMeTAD, 14.5 μL of 4-tert-butylpyridine (tBP), and 9.5 μL of a 520 mg mL⁻¹ lithium trifluoromethanesulfonyl (Li-TFSI) in acetonitrile with 1 mL of chlorobenzene. The Spiro-OMeTAD solution was spin-coated onto the antimony selenide film at 3000 r/min for 30 s and baked at 105°C for 10 min. A 60 nm-thick Au back electrode was then deposited via thermal evaporation. Finally, the active device area was defined as 0.04 cm² using a metallic mask.

## Acknowledgements

## Declaration of conflicting interests

The authors declare no conflicting interests regarding the content of this article.

**Electronic Supplementary Material**: Supplementary material is available in the online version of this article at https://doi.org/10.26599/EMD.2024.9370027.

## References

[1]  Green, M. A., Dunlop, E. D., Siefer, G., Yoshita, M., Kopidakis, N., Bothe, K., Hao, X. J. (2023). Solar cell efficiency tables (Version 61). *Prog. Photovoltaics: Res. Appl.* 31, 3–16.

[2]  Shockley, W., Queisser, H. J. (1961). Detailed balance limit of efficiency of p-n junction solar cells. *J. Appl. Phys.* 32, 510–519.

[3]  De Vos, A. (1980). Detailed balance limit of the efficiency of tandem solar cells. *J. Phys. D: Appl. Phys.* 13, 839–846.

[4]  Leijtens, T., Bush, K. A., Prasanna, R., McGehee, M. D. (2018). Opportunities and challenges for tandem solar cells using metal halide perovskite semiconductors. *Nat. Energy* 3, 828–838.

[5]  Chen, C., Li, K. H., Tang, J. (2022). Ten years of Sb₂Se₃ thin film solar cells. *Solar RRL* 6, 2200094.

[6]  Cai, H. L., Cao, R., Gao, J. X., Qian, C., Che, B., Tang, R. F., Zhu, C. F., Chen, T. (2022). Interfacial engineering towards enhanced photovoltaic performance of Sb₂Se₃ solar cell. *Adv. Funct. Mater.* 32, 2208243.

[7]  Yeom, K. M., Kim, S. U., Woo, M. Y., Noh, J. H., Im, S. H. (2020). Recent progress in metal halide perovskite-based tandem solar cells. *Adv. Mater.* 32, 2002228.

[8]  Jin, Y. B., Feng, H. P., Fang, Z., Yang, L., Liu, K. K., Deng, B. R., Chen, J. F., Chen, X. L., Zhong, Y. W., Yang, J. X., et al. (2023). Stabilizing semi-transparent perovskite solar cells with a polymer composite hole transport layer. *Nano Res.* in press. https://doi.org/10.1007/s12274-023-5975-5

[9]  Kim, J. H., Seok, H. J., Seo, H. J., Seong, T. Y., Heo, J. H., Lim, S. H., Ahn, K. J., Kim, H. K. (2018). Flexible ITO films with atomically flat surfaces for high performance flexible perovskite solar cells. *Nanoscale* 10, 20587–20598.

[10]  Dkhissi, Y., Huang, F. Z., Rubanov, S., Xiao, M. D., Bach, U., Spiccia, L., Caruso, R. A., Cheng, Y. B. (2015). Low temperature processing of flexible planar perovskite solar cells with efficiency over 10%. *J. Power Sources* 278, 325–331.

[11]  Roldán-Carmona, C., Malinkiewicz, O., Soriano, A., Espallargas, G. M., Garcia, A., Reinecke, P., Kroyer, T., Dar, M. I., Nazeeruddin, M. K., Bolink, H. J. (2014). Flexible high efficiency perovskite solar cells. *Energy Environ. Sci.* 7, 994–997.

[12]  Schultes, M., Helder, T., Ahlswede, E., Aygüler, M. F., Jackson, P., Paetel, S., Schwenzer, J. A., Hossain, I. M., Paetzold, U. W., Powalla, M. (2019). Sputtered transparent electrodes (IO:H and IZO) with low parasitic near-infrared absorption for perovskite–Cu(In, Ga)Se₂ tandem solar cells. *ACS Appl. Energy Mater.* 2, 7823–7831.

[13]  Xu, W. Z., Gao, Y., He, M., Chen, S. Y., Fu, H. Y., Wei, G. D. (2023). Functional polymer passivating FA₀.₈₅PEA₀.₁₅SnI₃ for efficient and stable lead-free perovskite solar cells. *Nano Res.* 16, 481–488.

[14]  Zhang, X., Zhang, H., Li, S. L., Xiao, L. G., Zhang, S. W., Han, B., Kang, J. J., Zhou, H. Q. (2023). Development and application of blade-coating technique in organic solar cells. *Nano Res.* 16, 11571–11588.

[15]  Liu, X. X., Zhang, J. J., Tang, L. T., Gong, J. B., Li, W., Ma, Z. Y., Tu, Z. X., Li, Y. Y., Li, R. M., Hu, X. Z., et al. (2023). Over 28% efficiency perovskite/Cu(InGa)Se₂ tandem solar cells: highly efficient sub-cells and their bandgap matching. *Energy Environ. Sci.* 16, 5029–5042.

[16]  Guchhait, A., Dewi, H. A., Leow, S. W., Wang, H., Han, G. F., Suhaimi, F. B., Mhaisalkar, S., Wong, L. H., Mathews, N. (2017). Over 20% efficient CIGS–perovskite tandem solar cells. *ACS Energy Lett.* 2, 807–812.

[17]  Kamat, P. V. (2018). Hybrid perovskites for multijunction tandem solar cells and solar fuels. A virtual issue. *ACS Energy Lett.* 3, 28–29.

[18]  Zhou, Y., Wang, L., Chen, S. Y., Qin, S. K., Liu, X. S.,

Chen, J., Xue, D. J., Luo, M., Cao, Y. Z., Cheng, Y. B., et al. (2015). Thin-film Sb$_2$Se$_3$ photovoltaics with oriented one-dimensional ribbons and benign grain boundaries. *Nat. Photonics* 9, 409–415.

[19] Liu, X. S., Chen, J., Luo, M., Leng, M. Y., Xia, Z., Zhou, Y., Qin, S. K., Xue, D. J., Lv, L., Huang, H., et al. (2014). Thermal evaporation and characterization of Sb$_2$Se$_3$ thin film for substrate Sb$_2$Se$_3$/CdS solar cells. *ACS Appl. Mater. Interfaces* 6, 10687–10695.

[20] Wen, X. X., Chen, C., Lu, S. C., Li, K. H., Kondrotas, R., Zhao, Y., Chen, W. H., Gao, L., Wang, C., Zhang, J., et al. (2018). Vapor transport deposition of antimony selenide thin film solar cells with 7.6% efficiency. *Nat. Commun.* 9, 2179.

[21] Mavlonov, A., Razykov, T., Raziq, F., Gan, J. T., Chantana, J., Kawano, Y., Nishimura, T., Wei, H. M., Zakutayev, A., Minemoto, T., et al. (2020). A review of Sb$_2$Se$_3$ photovoltaic absorber materials and thin-film solar cells. *Sol. Energy* 201, 227–246.

[22] Mamta, Singh, Y., Maurya, K. K., Singh, V. N. (2021). A review on properties, applications, and deposition techniques of antimony selenide. *Sol. Energy Mater. Sol. Cells* 230, 111223.

[23] Zeng, K., Xue, D. J., Tang, J. (2016). Antimony selenide thin-film solar cells. *Semicond. Sci. Technol.* 31, 063001.

[24] Jiang, C. H., Yao, J. S., Huang, P., Tang, R. F., Wang, X. M., Lei, X. Y., Zeng, H. L., Chang, S., Zhong, H. Z., Yao, H. B., et al. (2020). Perovskite quantum dots exhibiting strong hole extraction capability for efficient inorganic thin film solar cells. *Cell Rep. Phys. Sci.* 1, 100001.